Article

Quantification Method of Driving Risks for Networked Autonomous Vehicles Based on Molecular Potential Fields

Yicheng Chen, Dayi Qu *, Tao Wang ![ORCID], Shanning Cui and Dedong Shao

College of Civil Engineering, Qingdao University of Technology, Qingdao 266520, China;
cyc30144701@163.com (Y.C.); wangtaoqd1987@163.com (T.W.); loser365@163.com (S.C.);
sdd332024949@163.com (D.S.)
* Correspondence: dayiqu@qut.edu.cn

Abstract: Connected autonomous vehicles (CAVs) face constraints from multiple traffic elements, such as the vehicle, road, and environmental factors. Accurately quantifying the vehicle's operational status and driving risk level in complex traffic scenarios is crucial for enhancing the efficiency and safety of connected autonomous driving. To continuously and dynamically quantify the driving risks faced by CAVs in the road environment—arising from the front, rear, and lateral directions—this study focused s on the self-driving particle characteristics that enable CAVs to perceive their surrounding environment and make driving decisions. The vehicle-to-vehicle interaction behavior was analogized to the intermolecular interaction relationship, and a molecular Morse potential model was applied, coupled with the vehicle dynamics theory. This approach considers the safety margin and the specificity of driving styles. A multi-layer decoder–encoder long short-term memory (LSTM) network was employed to predict vehicle trajectories and establish a risk quantification model for vehicle-to-vehicle interaction behavior. Using SUMO software (win64-1.11.0), three typical driving behavior scenarios—car-following, lane-changing, and yielding—were modeled. A comparative analysis was conducted between the risk field quantification method and existing risk quantification indicators such as post-encroachment time (PET), deceleration rate to avoid crash (DRAC), modified time to collision (MTTC), and safety potential fields (SPFs). The evaluation results demonstrate that the risk field quantification method has the advantage of continuously quantifying risk, addressing the limitations of traditional risk indicators, which may yield discontinuous results when conflict points disappear. Furthermore, when the half-life parameter is reasonably set, the method exhibits more stable evaluation performance. This research provides a theoretical basis for the dynamic equilibrium control of driving risks in connected autonomous vehicle fleets within mixed-traffic environments, offering insights and references for collision avoidance design.

Keywords: vehicle-to-vehicle interaction; risk quantification; molecular potential fields; networked autonomous vehicles; deep learning

1. Introduction

Traffic safety remains a paramount concern that the transportation system must address. The World Health Organization's Global Road Safety Status Report states that road traffic accidents are the eighth leading cause of death, with 1.35 million people dying each year globally due to traffic accidents. Moreover, the vast majority of these accidents are caused by vehicle collisions [1]. Prior to formulating various strategies to prevent vehicular collisions, it is essential to accurately assess the potential risks surrounding vehicles. This

not only significantly reduces the likelihood of accidents, but also enhances the efficiency of road traffic. Generally speaking, the assessment of potential road risks is achieved through traffic risk indicators, which are traditionally categorized into three types: time-based risk indicators, distance-based risk indicators, and deceleration-based indicators. In practical applications, time-based risk indicators are the most widely utilized, such as time to collision (TTC) [2], time exposed to collision (TET) [3], and modified time to collision (MTTC) [4]. Distance-based risk indicators, such as headway time (H) [5], are primarily employed to calculate the safe distance required to avert collisions. Deceleration-based indicators assess driving risks in emergency situations based on deceleration rates, such as conflict speed (CS) [6]. Although these safety surrogate indicators are widely used in conflict quantification studies across various traffic scenarios, they also have certain limitations: (1) traditional safety surrogate indicators do not account for the driver's reaction characteristics; (2) constraints of boundary conditions, such as traditional TTC-based indicators failing to quantify rear-end collision risks when "the following vehicle's speed is less than that of the leading vehicle"; (3) the uncertainty in the risk level classification thresholds also leads to deviations in the risk quantification results. To address the limitations of single risk quantification indicators, this study comprehensively analyzes the vehicle kinematic mechanisms and the driver's reaction characteristics. It introduces the concept of the driver behavior molecular potential field to systematically describe the distribution of traffic flow risks, the degree of response to the traffic environment, and the dynamic relationship between these factors.

The structure of the article is as follows: Section 1 presents existing quantification indicators for vehicular driving risks. Section 2 discusses recent research in the field of transportation based on field theory. Section 3 draws an analogy between vehicles and self-driven particles from the perspective of molecular force fields, establishing relevant models for the quantification of driving risks. Section 4 validates the feasibility of the proposed methods by applying a vehicle trajectory prediction model. Section 5 outlines the experimental setup and data processing procedures. Section 6 showcases the assessment results of the driving risks using this method. Section 7 concludes the paper.

2. Literature Review

In recent years, vehicle interaction models based on the field theory have garnered significant attention due to their objectivity, versatility, flexibility, and interpretability. Li et al. [7] proposed a simplified stimulus–response car-following model based on artificial potential fields, which was validated using the NGSIM dataset, revealing a new direction for addressing vehicle control issues that balance safety in complex traffic environments. Liu et al. [8] modeled traffic factors such as lane markings and connected vehicles to construct a control model for autonomous vehicles, demonstrating its effectiveness. Li et al. [9] established a car-following model grounded in the driving risk field theory and validated its efficacy through numerical simulations, subsequently proposing a novel risk perception warning strategy to mitigate driving risks for connected autonomous vehicles. Wang et al. [10] introduced a driving safety potential field that characterizes the comprehensive risks associated with drivers, connected vehicles, and roadways. Qin et al. [11] investigated the impact of connected auxiliary devices on the efficiency of mixed-traffic flow. Jia et al. [12] combined the Lennard–Jones potential function with safety potential fields, incorporating acceleration parameters and considering the combined effects of lane markings and road boundaries to develop an optimized safety potential car-following model in connected environments, validated using the Shanghai natural driving research dataset. Qu et al. [13] approached the problem from a molecular force field perspective, introducing a velocity coordination term to propose a new framework for systematically

analyzing the collaborative relationships and safety dynamics of heterogeneous connected vehicle groups.

Similarly, Ma et al. designed an emergency takeover scenario on urban expressways, utilizing a risk field to assess the risk for experimental vehicles. This approach effectively analyzed the driving risks during the takeover process of L3 autonomous vehicles under different cognitive levels. The results indicate that the model outperforms TTC in terms of accuracy in representing risk [14]. In order to understand the dynamic characteristics of surrounding vehicles and avoid potential driving risks in mixed traffic, Huang et al. proposed a probabilistic driving risk assessment framework based on driving intent recognition and vehicle risk evaluation within the system. An LSTM network was used to build the intent recognition model to identify the driving intentions of surrounding vehicles, and then the driving safety field theory was applied to output potential risks [15]. Zheng et al. conducted a predictive study on future driving risks by reading historical vehicle trajectory data to calculate the relative position and future motion trajectory of the target vehicle with respect to the experimental vehicle. The simulation results indicate the safety, continuity, and dynamic feasibility of the proposed algorithm [16]. Chen et al. also considered both comfort and safety, setting up static and dynamic risk fields. By selecting the optimal driving trajectory, they achieved lane-change optimization, ensuring that passengers were in a comfortable state for 97.5% of the time during the lane-change process [17].

In summary, existing research on driving safety fields and risk quantification theories is primarily based on the field theory, utilizing artificial potential fields to analyze driving safety issues in the human–vehicle–road system, achieving substantial results. However, some studies conducted in intelligent connected environments lack a comprehensive consideration of vehicle dynamics, driver psychological characteristics, and the interactions between multiple vehicles. In contrast to the basic field theory, this study is grounded in the Morse molecular field theory, which simultaneously considers the impact of both the physiological and psychological characteristics of the driver on driving safety, as well as the complex and dynamic traffic environment. This approach enables a more accurate description of the coupling mechanisms between humans, vehicles, and roads, taking into account the time–space risk field superposition effects caused by different factors such as vehicle position, speed, and acceleration. A novel visual risk quantification method is proposed for the connected mixed-traffic environment, offering stable and precise risk assessment in the complex human–machine co-driving traffic scenarios.

3. Molecular Force Field Description and Modeling

Molecular force refers to the attractive and repulsive forces between molecules. Specifically, when the distance between molecules is less than the equilibrium distance, they exhibit repulsive forces; when the distance exceeds the equilibrium distance, attractive forces prevail; and when the distance surpasses the escape distance, they enter a state of freedom. The interaction between two vehicles mirrors molecular behavior. In 1929, physicist Philip Morse [18] introduced a potential energy function to describe the interactions between atoms or molecules, known as the Morse potential. This function has been widely applied in fields such as molecular spectroscopy, molecular dynamics, and the calculation of molecular energy levels, and can be expressed as follows:

$$U_{\text{morse}(r)} = D\Big\{ \{1 - \exp[-p(r - r_0)]\}^2 - 1 \Big\} \tag{1}$$

In the equation, $U_{\text{morse}(r)}$ represents the strength of the Morse force field, p denotes a variable parameter, r indicates the distance between molecules, r_0 signifies the equilibrium distance between molecules, and D represents the dissociation energy between the

molecules. The potential function exhibits a double-well shape reminiscent of that of a harmonic oscillator. Once the distance between molecules exceeds the equilibrium distance, the potential energy decays at an accelerated rate, thus providing a more precise depiction of molecular vibrational phenomena. The strength of the Morse force field varies with p and r_0, as illustrated in Figure 1.
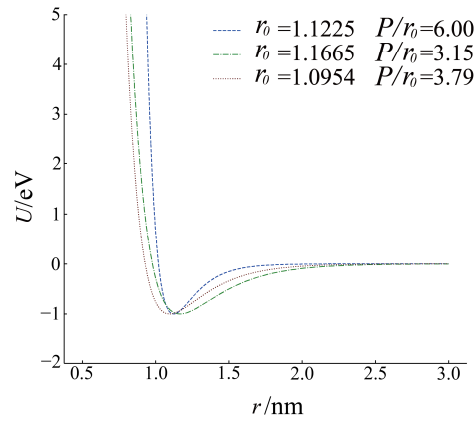

Figure 1. Trends in the Morse potential field.

From a physics perspective, a field can be understood as the interaction force that an object with specific properties exerts on other objects within a defined spatial range, without direct surface contact. The magnitude of this interaction force varies depending on the relative positions of the objects. Consequently, the objects, due to their mutual interaction forces, possess potential energy that is related to their relative positions. Thus, a force field can be regarded as a description of the interaction capacity within the entire space surrounding an object. Similarly, a comparable physical field exists within transportation systems. The behavior of a vehicle, which seeks to maintain an optimal distance from the vehicle ahead—neither too close nor too far—can be viewed as the process by which the vehicle, under the influence of the "force field" of the leading vehicle, continuously adjusts its speed through acceleration or deceleration to achieve the following equilibrium. In the context of intelligent and connected transportation systems, as CAVs (connected and autonomous vehicles) become more prevalent in the future, driving authority will transition from human drivers to autonomous vehicle decision-making. Each factor influencing vehicle motion can be considered a field source within its spatial domain, with the risk field being the result of the superposition of these field sources. Therefore, the Morse risk field can be understood as a physical field reflecting the impact of traffic factors on driving safety. In an intelligent connected environment, conditions are conducive to acquiring parameters such as differences in vehicle speed, velocity, and acceleration. Accordingly, we introduced the equilibrium distance l_0 between vehicles, corresponding to the intermolecular equilibrium distance r_0, and employed the Morse potential to characterize the interactive risk force field among vehicles.

$$l_0 = \lambda_0(\lambda_1 - \lambda_2 \Delta v - \lambda_3 \Delta a)v_n \tag{2}$$

In the equation, l_0 represents the equilibrium distance between vehicles; Δv denotes the speed difference between the target vehicle and the interacting vehicle; Δa signifies the acceleration difference between the target vehicle and the interacting vehicle; v_n indicates the speed of the target vehicle; and λ_0, λ_1, λ_2, and λ_3 represent the comprehensive influence parameters of speed, speed difference, and acceleration difference. By integrating Equations (1) and (2), we constructed the vehicle interaction field as follows:

$$U(l) = l_m \left\{ \{1 - \exp[-\beta l + \lambda_0 v_n(\lambda_1 - \lambda_2 \Delta v - \lambda_3 \Delta a)]\}^2 - 1 \right\} \tag{3}$$

In the equation, l_m denotes the maximum interaction distance between vehicles, l represents the distance between vehicles, and β is the field parameter. Building upon this, we applied the gradient descent method to derive the force function acting on the target vehicle as follows:

$$F(l) = -\frac{dU(l)}{dl} = -2\beta l_m\{1 - \exp[-\beta(l - l_0)]\}\exp[-\beta(l - l_0)] \tag{4}$$

Furthermore, we can derive the acceleration of the target vehicle induced by the interaction force field as follows:

$$a = \frac{2\beta l_m\{\exp[-\beta(l - l_0)] - 1\}\exp[-\beta(l - l_0)]}{M} \tag{5}$$

In the equation, M represents the mass of the target vehicle. Based on the vehicle interaction force field, we can derive the potential risk field associated with vehicle interactions as follows:

$$U_V = l_m\left\langle \{1 - \exp[-\beta l + \lambda_0 v_n(\lambda_1 - \lambda_2\Delta v - \lambda_3\Delta a)]\}^2 - 1\right\rangle \cdot \omega \cdot \exp(\cos\theta) \tag{6}$$

In the equation, θ denotes the angle between the vehicle's velocity direction and the road's centerline, while ω represents the field parameter.

To integrate spatial and temporal risks, while distinguishing the impact of varying future time on the risk field, we introduced the discount function $\gamma(t)$. This discount function adheres to the principle of half-life, exhibiting an exponential decay in its value as the future time unit progresses.

$$\gamma(t) = (0.5)^{t/t_{1/2}} \tag{7}$$

In the equation, $t_{1/2}$ represents the half-life, indicating the driver's level of concern regarding future risks. A larger value of A signifies a slower decay of the risk field across spatial dimensions, reflecting a heightened awareness of long-term future risks by the driver; t denotes the future time variable.

From Equations (6) and (7), we can derive the potential spatiotemporal risk field of vehicle interactions as follows:

$$U_r = l_m\left\{ \{1 - \exp[-\beta l + \lambda_0 v_n(\lambda_1 - \lambda_2\Delta v - \lambda_3\Delta a)]\}^2 - 1\right\} \cdot \omega \cdot \exp(\cos\theta) \cdot (0.5)^{t/t_{1/2}} \tag{8}$$

In order to more accurately describe the risk zone, it is essential to consider the actual occupied area of each vehicle. The actual occupied area refers not only to the physical space occupied by the vehicle on the road, but also its safety margin.

Nilsson R [19] describes the safety margin as the "distance that causes a perceived threat to the driver", which represents the vehicle dimensions as perceived by the driver. It is the additional space allocated to the vehicle, providing the driver with a greater sense of safety and comfort during operation. Furthermore, it helps compensate for measurement errors in onboard and road-based sensors to some extent, thereby aiding in making more conservative risk predictions. Therefore, the safety margin is expressed as the maximum interaction distance (l_m) between the target vehicle and the interacting vehicle, as follows:

$$l_m = V_R \cdot (\tau_1 + \tau_2) + \frac{V_R^2}{2a_R} - \frac{V_F^2}{2a_F} - D_R \tag{9}$$

In the equation, V_R represents the speed of the target vehicle, while V_F denotes the speed of the interactive vehicle. τ_1 refers to the driver's response time, which is the amount of time it takes for the driver to react after perceiving a potential risk. τ_2 stands for the

braking system's response time, which is the time delay between the driver's or automated system's braking command and the actual response of the braking system. a_R indicates the acceleration of the target vehicle, describing how quickly the target vehicle accelerates or decelerates. a_F represents the acceleration of the interactive vehicle, reflecting how fast the interacting vehicle accelerates or decelerates. Finally, D_R is the relative distance between the two vehicles, representing the distance between the target and interactive vehicles at a given moment.

The different motion states of a vehicle and its interaction with other vehicles can influence the distribution of the risk field. The risk field distribution of a vehicle at a given moment is discussed in three typical scenarios below. When the vehicle is driving freely at a constant speed, the risk field reaches its peak within its safety margin and gradually decreases as the distance increases, as shown in Figure 2. When the vehicle is in a following state, the risk potential has a saddle-shaped distribution, with the risk field in the area between the two vehicles significantly higher than in the front of the lead vehicle and the rear of the following vehicle, as shown in Figure 3. When the vehicle is in a lane-changing state, the risk field is superimposed along the direction of the vehicle's movement, but it still peaks within its safety margin, as shown in Figure 4.
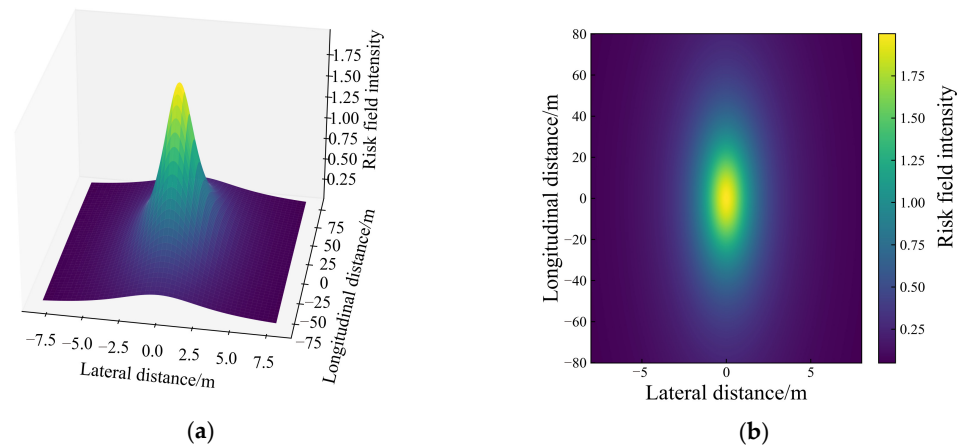

(a)　　　　　　　　(b)

Figure 2. Vehicle-free travel risk field distribution. (**a**) Three-dimensional distribution of the field strength. (**b**) Field strength plane distribution.
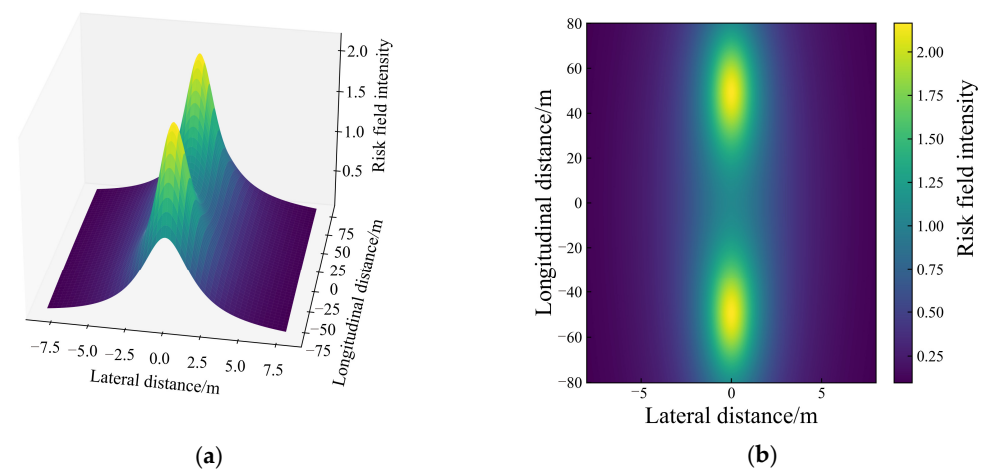

(a)　　　　　　　　(b)

Figure 3. Vehicle following driving risk field distribution. (**a**) Three-dimensional distribution of the field strength. (**b**) Field strength plane distribution.
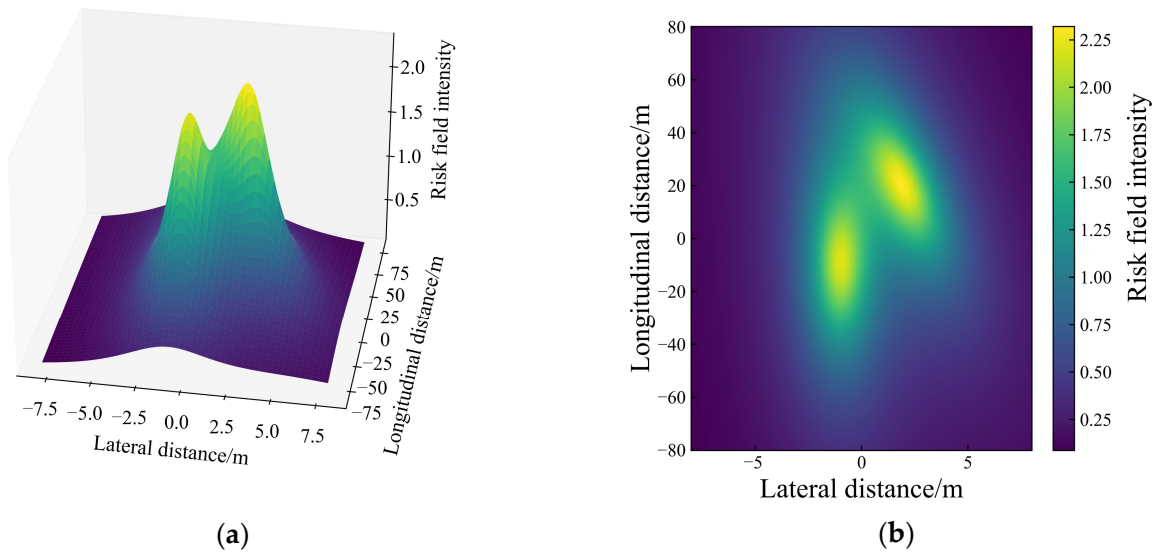
(**a**)

(**b**)

Figure 4. Distribution of the risk fields for vehicle lane changing behavior. (**a**) Three-dimensional distribution of the field strength. (**b**) Field strength plane distribution.

4. Vehicle Trajectory Prediction Model

Considering the impact of driver heterogeneity on the risk field, a deep learning neural network was applied to predict the short-term future position of the vehicle, and a vehicle trajectory risk field was constructed by integrating multidimensional factors.

4.1. Input and Output

The input and output of the prediction model are denoted as X and Y, respectively, as shown in Equation (10). T_h and τ represent the observation time for the input and the prediction time range for the output, respectively. During the input phase, parameters such as the vehicle's position, speed, acceleration, and steering angle were recorded with a time step of 0.1 s, until T_h was reached. In the prediction phase, the vehicle's motion parameters are predicted using the same time step of 0.1 s, until τ was reached.

$$\begin{cases} X = X_{t-T_h}, X_{t-T_h+1}, \cdots, X_t; \\ Y = Y_{t+j}, j = 1, 2, \cdots, \tau; \end{cases} \tag{10}$$

$$\begin{cases} X_t = \left[x_{t-p}^k, y_{t-p}^k\right], k \in [1, 2, \cdots, N], p \in [0, 1, 2, \cdots, T_h]; \\ Y_{t+j} = \left[x_{t+q}^k, y_{t+q}^k\right], k \in [1, 2, \cdots, N], q \in [0, 1, 2, \cdots, \tau]. \end{cases} \tag{11}$$

In the equation, X_t represents the input range and its dimensions (T_h time steps $\times x, y$ coordinates $\times$ number of vehicles), and Y_{t+j} represents the output range and its dimensions (τ time steps $\times x, y$ coordinates $\times$ number of vehicles).

4.2. Deep Learning EDLN Model

The encoder–decoder long short-term memory network (EDLN), as a variant of the long short-term memory (LSTM) recurrent neural network, has been shown by Ettinger et al. [20] to effectively extract trajectory features in complex scenarios. Therefore, EDLN was chosen as the basis for the prediction model, which is primarily divided into three components: the encoder, the decoder, and the mixture density layer, as shown in Figure 5. The encoder and decoder of the EDLN are composed of LSTM stacks with the same structure and weights [21–23]. The encoder transforms historical trajectory data into a bridging vector, storing the behavioral features of interacting vehicles, while the

decoder outputs the vehicle's *x* and *y* coordinate vectors based on the encoded features of the bridging vector. Finally, the mixture density layer outputs the predicted distribution of the vehicle.
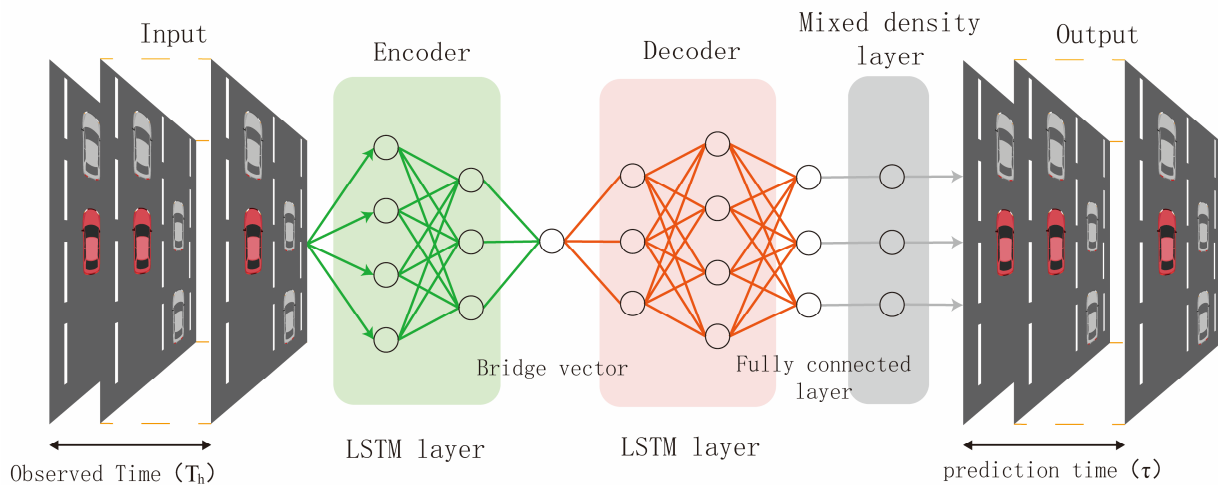

Figure 5. Deep learning predictive modeling flowchart.

Considering the prediction performance, the model uses two layers of LSTM, with a total of 512 neurons, and the initial learning rate was set to 0.001 [24–27]. The number of Gaussian distributions in the mixture density layer was set to 6. Since evaluating the prediction model was crucial for determining its effectiveness and reliability, the learning rate was halved if the validation loss did not improve within 5 epochs. To prevent overfitting, training was stopped and the trained model was saved if the validation loss did not improve within 10 epochs.

5. Data Processing and Simulation Experiment Setup

The experiment used the CitySim dataset from the Intelligent Transportation Safety Laboratory (UCF-SST) at the University of Central Florida, with a total duration of 1200 min, including driving trajectory data for over 10,000 vehicles [28]. After visualizing and analyzing the vehicle trajectories, it was found that the data from the Expressway A urban expressway interwoven section exhibited concentrated distributions of driving behaviors such as vehicle following and lane changing. To effectively quantify the risk of various interactive behaviors of vehicles in complex traffic environments, this section was selected to validate the accuracy of the trajectory prediction model and the effectiveness of the risk quantification method. Considering the computational capacity of the equipment, the input observation time (T_h) was set to 1 s, the prediction time range (τ) was set to 6 s, and the risk field half-life ($t_{1/2}$) was set to 0.5 s.

5.1. Data Processing

Due to the presence of noisy data (sudden changes in speed and acceleration) in the original CitySim dataset, as shown in the gray area of Figure 6, which may lead to anomalous vehicle trajectories, abnormal acceleration data exceeding the acceleration threshold were filtered out during the data processing. When the original data's acceleration exceeded the threshold, linear interpolation was used to denoise the two adjacent data points. Additionally, a moving average filter with a duration of 0.5 s was applied to reduce the impact of random noise. The denoised data are represented by the dashed line in Figure 6 [29–32].
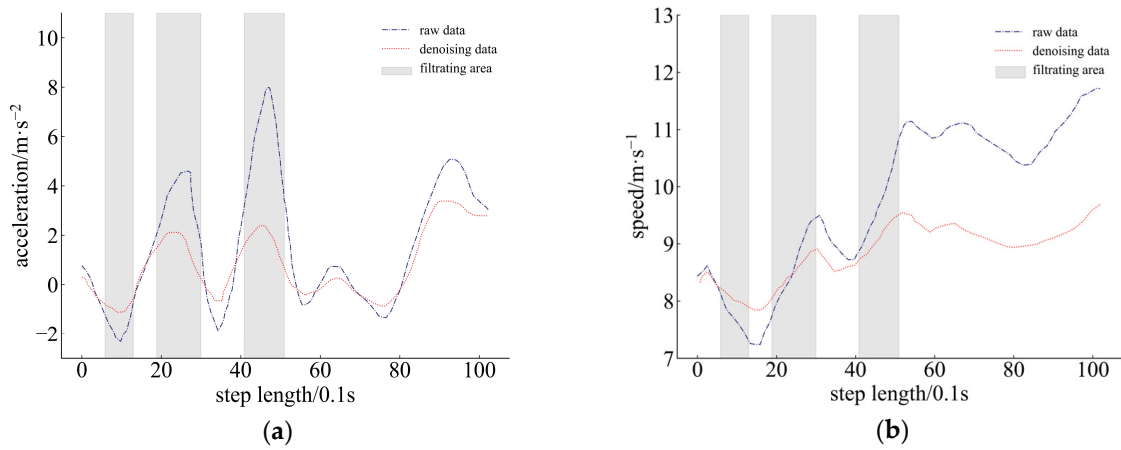
Figure 6. Comparative analysis of raw data and denoised data. (**a**) Comparative analysis of acceleration data. (**b**) Comparative analysis of speed data.

5.2. Simulation Experiment Setup

To define the experimental objects and scope, a reference coordinate system consisting of at most seven vehicles was established. The target vehicle's coordinates were set at (0, 0), and the interaction vehicles are selected within a range where the center of the vehicle is located within a rectangle defined by X (−10, 10) and Y (−20, 80). The target vehicle is denoted as SV, the lead vehicle is marked as L, and the following vehicle is marked as F. The lane of the target vehicle is marked as 1, the left lane as 0, and the right lane as 2. The system consists of the target vehicle as the reference point and up to 6 surrounding interaction vehicles. The positions were recorded every 0.1 s, and each set of records was defined as one observation. The observations of non-interacting vehicles were filtered out.

After conducting a continuous 10 min recording of the Expressway A section from the CitySim dataset, 12,284 observation data points were selected and divided into two groups: 80% of the data, after processing, was used as the training set for training the deep learning trajectory prediction model, and 20% was used as the test set.

During the setup of the test scenario, the SUMO software was used to create a -km long, one-way, three-lane highway. It included two typical vehicle interaction scenarios (car-following and lane-changing) to evaluate the applicability of the risk quantification model. In the vehicle following scenario, as shown in Figure 7a, the target vehicle was behind the interaction vehicle and remains in the same lane, with a longitudinal conflict risk. In the lane changing scenario, as shown in Figure 7b, the target vehicle was ahead of the interaction vehicle and was in an adjacent lane. The target vehicle was changing from its lane to the lane of the interaction vehicle, and both longitudinal and lateral conflict risks were present.
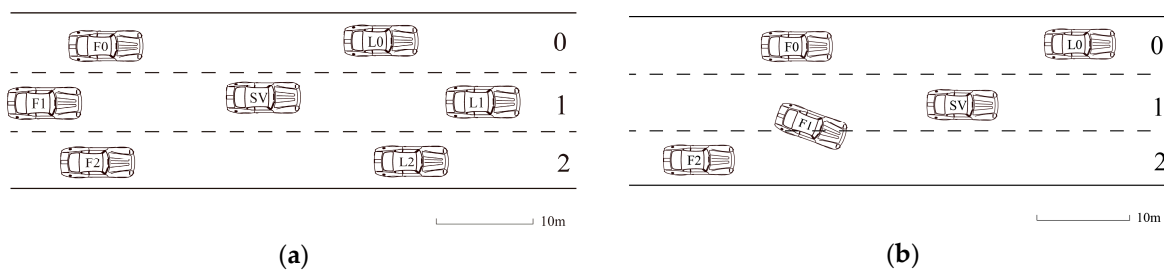

Figure 7. SUMO test scenarios. (**a**) Car following scene. (**b**) Changing lane scene.

6. Discussion

6.1. Risk Quantification Method Evaluation

We applied the Morse risk field (*MRF*) quantification model to continuously calculate the interaction vehicle risk field intensity at fixed intervals across different driving scenarios. In the microscopic car following scenario, which involves only one target vehicle and one interaction vehicle, the interaction vehicle drives directly in front of the target vehicle, undergoing acceleration, constant speed, deceleration, and constant speed movements sequentially. The target vehicle follows the interaction vehicle. The results of the car following scenario experiment are shown in Figure 8. Figure 8a displays the speed of each vehicle and the driving risk experienced by the target vehicle. v_1 represents the speed of the interaction vehicle, v_2 represents the speed of the target vehicle, and *MRF* represents the driving risk the target vehicle experiences from the interaction vehicle. Figure 8b shows the driving risk experienced by the target vehicle, where TTC^{-1} indicates the inverse of the time to collision between the two vehicles, *MRF* represents the driving risk the target vehicle experiences from the interaction vehicle, *MRF-c* indicates the driving risk the target vehicle experiences from the interaction vehicle at the current moment, and *MRF-p* represents the predicted future driving risk the target vehicle will experience from the interaction vehicle.
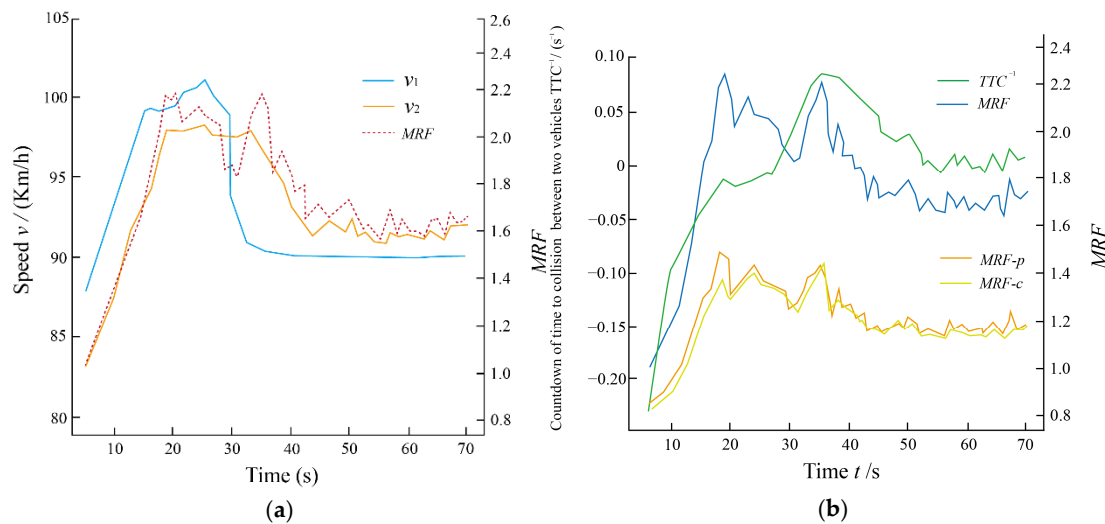

Figure 8. Experimental results of the car following scenario. (**a**) The speed of each vehicle and the driving risk experienced by the target vehicle in the car following scenario. (**b**) The driving risk experienced by the target vehicle in the car following scenario.

As can be seen from Figure 8b, the variation patterns of TTC^{-1} and *MRF* are generally similar, with the difference being that during the 18–30 s period, TTC^{-1} reflects a lower driving risk, while *MRF* indicates a higher risk. From Figure 8a, it is evident that the 18–30 s period corresponds to the high-speed car following phase, and after 45 s, it represents the medium-speed car following phase. TTC^{-1} reflects a consistent driving risk for the target vehicle during both phases, which does not align with the actual situation. In contrast, *MRF* shows a higher driving risk during the high-speed car following phase and a lower risk during the medium-speed car following phase. Therefore, in this scenario, *MRF* provides a more accurate representation of the driving risk than TTC^{-1}. Furthermore, Figure 8b illustrates the driving risk experienced by the target vehicle at the current moment (*MRF-c*), as well as the predicted future driving risk (*MRF-p*). The root mean square error between *MRF-c* and *MRF-p* was 0.052, with a deviation of 5.38%. From the figure, it can be observed that the variation patterns of *MRF-c* and *MRF-p* were consistent, with *MRF-p* located to the left of the *MRF-c* curve, indicating that the *MRF-p* curve can represent the predicted future

driving risk at the current moment. This demonstrates the effectiveness of the proposed model in the car following scenario.

In the merging scenario (involving only one target vehicle and one interacting vehicle), the target vehicle is traveling at approximately 82 km/h in the right lane, while the interacting vehicle accelerates from behind in the left lane, overtakes the target vehicle at about 97 km/h, then changes lanes to the right and merges into the target vehicle's lane. The results of the merging scenario experiment are shown in Figure 9. Figure 9a displays the speeds of the vehicles and the driving risk experienced by the target vehicle. Here, v_1 represents the speed of the interacting vehicle, v_2 represents the speed of the target vehicle, and MRF indicates the driving risk experienced by the target vehicle from the interacting vehicle. Figure 9b shows the relative distance between the vehicles and the driving risk experienced by the target vehicle. Specifically, d–x represents the lateral relative distance between the two vehicles, d–y represents the relative distance along the direction of vehicle travel, and *MRF* represents the driving risk experienced by the target vehicle from the interacting vehicle. *MRF-c* indicates the driving risk experienced by the target vehicle at the current moment, while *MRF-p* represents the predicted future driving risk experienced by the target vehicle from the interacting vehicle.
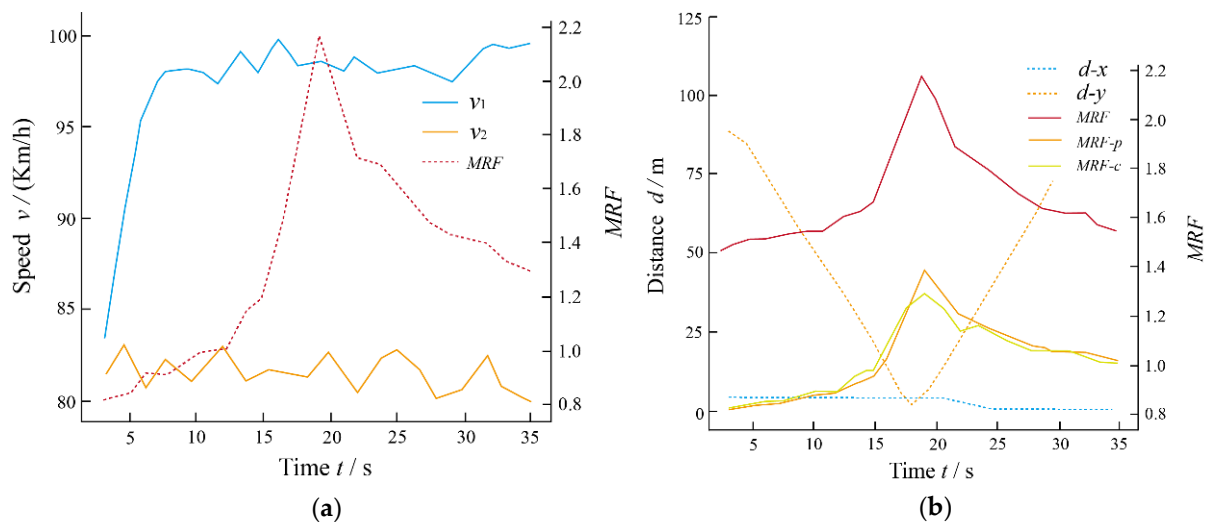

Figure 9. Experimental results of the merging scenario. (**a**) The speed of the vehicles and the driving risk of the target vehicle in the merging scenario. (**b**) The relative distance between vehicles and the driving risk of the target vehicle in the merging scenario.

From Figure 9b, it can be observed that from 5 s to 17 s, as the relative distance between the two vehicles decreased, the driving risk experienced by the target vehicle significantly increased. After 17 s, as the relative distance increases, the driving risk decreases. Between 18 s and 21 s, the interacting vehicle changed lanes into the front lane of the target vehicle. Therefore, the region where the *MRF* decreased after 17 s can be divided into two phases: before and after the interacting vehicle merges. Prior to the merge, the *MRF* decreased at a faster rate because the interacting vehicle was positioned in the left front of the target vehicle; after the merge, the rate of decrease slowed, as the interacting vehicle was positioned directly in front of the target vehicle. At the same relative distance, the risk generated when the interacting vehicle was directly in front of the target vehicle is greater, which is consistent with real-world observations. Additionally, Figure 9b displays both the current driving risk (*MRF-c*) and the predicted future driving risk (*MRF-p*) for the target vehicle. The root mean square error between *MRF-c* and *MRF-p* was 0.08, and the deviation between *MRF-c* and *MRF-p* was 4.76%. It is evident from Figure 9b that the *MRF-c* and *MRF-p* exhibited consistent trends, with *MRF-p* lying to the left of the *MRF-c* curve. This

indicates that the *MRF-p* curve can represent the predicted future driving risk at the current moment, thus validating the effectiveness of the proposed model in the merging scenario.

Due to space limitations, a 6 s lane change scenario involving the target vehicle and six other interacting vehicles was selected for detailed illustration, as shown in Figure 10. During the entire process, the target vehicle moved from the left lane to the middle lane (Figure 10b), and interacted with the other six vehicles, leading to a conflict (Figure 10c). Once the target vehicle completed the lane change, it transitioned to a following maneuver (Figure 10d). In Figure 10a, the variation in risk field intensity for each vehicle is depicted. To clearly display and distinguish the risk fields of each vehicle, Figure 10b–d shows the risk fields in front of the interacting vehicles and the front and rear regions of the target vehicle, with areas of a higher risk intensity highlighted.
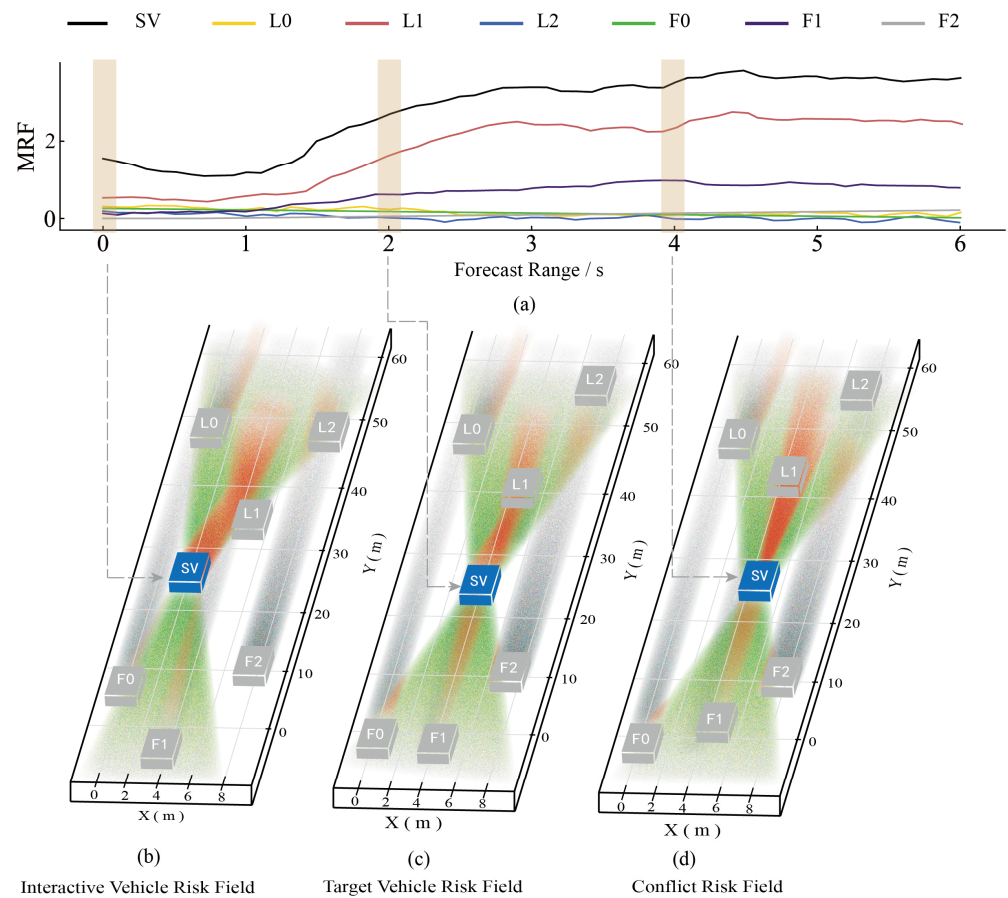

Figure 10. Comparative analysis of the target vehicle and interacting vehicle risk field changes in the forecast horizon.

6.2. Comparative Analysis with Existing Indicators

Existing risk quantification indicators primarily focus on evaluating single driving situations with conflict points. However, for scenarios where the risk is jointly influenced by the target vehicle and two or more interacting vehicles, current risk quantification indicators may not provide an effective assessment. Therefore, a comparative analysis was conducted between the *MRF* and existing conflict point-based risk quantification indicators (post-encroachment time, *PET*; modified time to collision, *MTTC*; deceleration rate to avoid crash, *DRAC*), as well as the safety field (safety potential field, *SPF*), which is also based on field theory. The results are shown in Figure 11.
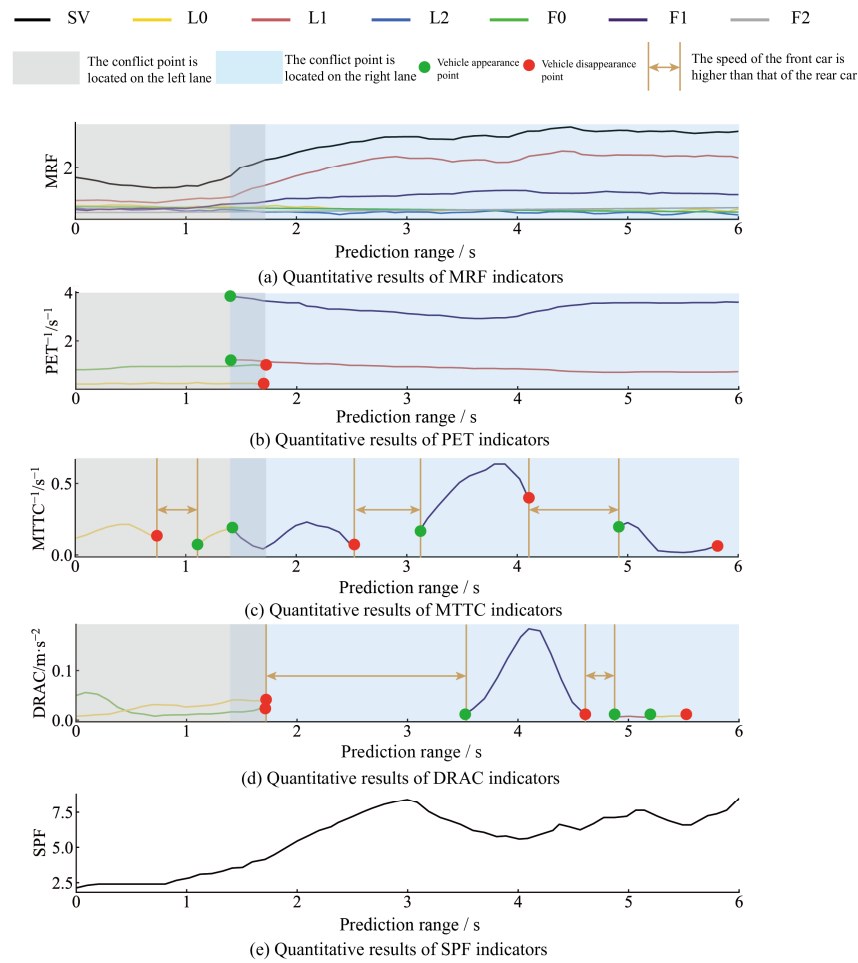
Figure 11. Results of the analysis of the quantitative indicators for each risk.

In Figure 11a, when the target vehicle started to change lanes around 1 s, its *MRF* gradually increased. Prior to the formation of conflict points with the forward-interacting vehicles (L0, L1, L2), the associated risk could be continuously quantified. From 1 to 4 s, during the lane change, no significant sudden changes in the *MRF* were observed. After approximately 4 s, once the lane change was completed, the vehicle entered the following state. Since the risk of longitudinal collision with L1 is relatively high, the *MRF* remained at a higher level.

In Figure 11b–d, marked points represent the moments of appearance and disappearance of vehicle trajectory conflict points. Traditional conflict point-based risk quantification indicators can only assess risks when conflict points appear on the predicted vehicle trajectories. In cases where the leading vehicle's speed is higher than that of the following vehicle, these traditional indicators fail to provide a continuous risk evaluation throughout the driving process.

As shown in Figure 11b, before the target vehicle completed the lane change, 1/*PET* could only evaluate the risk related to the two interacting vehicles (L0, F0) in the original lane. After the target vehicle completed the lane change, it only evaluated the risk related to the two interacting vehicles (L1, F1) in the target lane.

When the speed of the leading vehicle exceeded that of the following vehicle, as shown in Figure 11c,d, both 1/*MTTC* and *DRAC* indicators also showed limitations. In following situations, the headway and speed differential between the two vehicles may both be small. If the leading vehicle suddenly decelerated, the following vehicle had no opportunity to avoid the collision risk through deceleration or lane change. Therefore, in such cases, the Morse field risk quantification method based on the field theory has the advantage of

continuous risk quantification, compensating for the shortcomings of traditional conflict point-based risk indicators.

The method was compared with the safety potential field, which is also based on the field theory. By comparing Figure 11a,e, it can be observed that the overall trend of *SPF* was generally similar to that of *MRF*. However, *SPF* exhibited two significant fluctuations around 3 s (during the target vehicle's lane change process) and around 4 s (when switching from the lane change state to the following state). The former may be due to the consideration of lane markings, as the risk associated with the target vehicle crossing the lane lines differed before and after the lane change. The latter may arise because *SPF* only explores the spatial distance's effect on the field, without considering the field's temporal decay process. In contrast, the Morse field risk quantification method incorporates a half-life parameter ($t_{1/2}$) in Equation (7), allowing it to combine both spatial and temporal dimensions, thereby making the risk quantification results more aligned with the objective reality.

6.3. The Impact of Half-Life Parameters

The half-life parameter represents the driver's attention to future risks, and its value is of crucial importance. An excessively small value may reduce the sensitivity to the risk field generated by interacting vehicles, while an excessively large value may cause the risk field to spread over a large area of the road, increasing the computational burden without significantly improving the accuracy of the risk quantification.

Figure 10 compares the risk field under two different values of half-life parameters. As shown in Figure 12a, at $t_{1/2} = 0.25$ s, the assessment range of the risk field only covered a total of about 30 m in front and behind the target vehicle. At this time, drivers with more aggressive styles may be in a more dangerous situation due to a lack of sufficient parking distance from the preceding vehicle. In contrast, when $t_{1/2}$ took 0.5 s, as shown in Figure 12b, the range of the vehicle's risk field was significantly larger than the previous situation, and the coverage and intensity of the conflict risk field were also wider and stronger than the former, leaning toward a more conservative driving style.
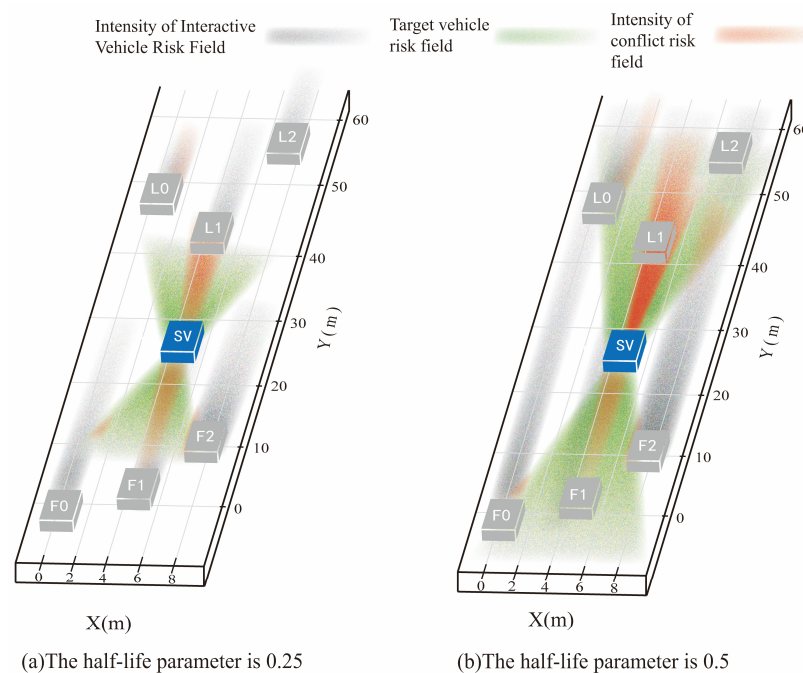

(a)The half-life parameter is 0.25   (b)The half-life parameter is 0.5

Figure 12. Effect of half-life parameters on the risk potential field.

7. Conclusions

Using the Morse molecular force field theory, the interaction relationships and underlying mechanisms between the target vehicle and adjacent vehicles are analyzed. The concept of risk fields is introduced, considering the time and spatial risk field superposition effects under the influence of various factors such as vehicle position, speed, and acceleration. A visualized risk quantification method is proposed for the connected and mixed traffic flow environment.

The risk quantification method can be applied to various interaction behaviors of vehicles in the same lane and across lanes (such as following and lane changing), ensuring that the risk assessment results exhibit smooth transitions at the start and end of driving behavior switches, and provide real-time risk levels faced by the target vehicle during these transitions.

The method quantitatively computes and visualizes the risk fields generated by the target vehicle and interacting vehicles. After comparing the proposed *MRF* index with *PET*, *MTTC*, *DRAC*, and *SPF*, it is found that the *MRF* index can compensate for the shortcomings of traditional risk quantification indicators, which may fail to provide continuous results at conflict points. Additionally, due to the introduction of the half-life parameter, the method can switch between more conservative and more aggressive risk assessments, allowing for a dynamic evaluation of the objective driving risks of drivers with different driving styles.

The results of interactive vehicle trajectory prediction were applied in the modeling of the driving risk field, enabling the prediction of the future trajectories of interacting vehicles. This allows the model to possess the capability to predict potential driving risks in future time periods. The deviation between predicted risks and actual risks was approximately 5%, indicating that this model can significantly enhance driving safety.

This study has certain limitations that require further improvement. The applicability of this method in more complex traffic scenarios needs to be further explored, as well as the impact of factors such as road width, curvature, and gradient on the quantification results. Building upon this research, a systematic, multi-dimensional, and comprehensive driving risk quantification framework could be established, providing a safer and more reliable driving environment for connected autonomous vehicles within intelligent connected mixed-traffic flows.

References

1. World Health Organization. *Global Status Report on Road Safety 2018*; World Health Organization: Geneva, Switzerland, 2018.
2. Bao, Z.Q.; Wu, L.; Zhai, W. Research on space-time layout optimization of right-turning vehicles and pedestrians at level intersection. *For. Eng.* **2022**, *38*, 156–163.
3. Minderhoud, M.M.; Bovy, P.H.L. Extended time-to-collision measures for road traffic safety assessment. *Accid. Anal. Prev.* **2001**, *33*, 89–97. [CrossRef] [PubMed]

4. Zheng, L.; Sayed, T.; Essa, M. Validating the bivariate extreme value modeling approach for road safety estimation with different traffic conflict indicators. *Accid. Anal. Prev.* **2019**, *123*, 314–323. [CrossRef] [PubMed]

5. Michael, P.G.; Leeming, F.C.; Dwyer, W.O. Headway on urban streets: Observational data and an intervention to decrease tailgating. *Transp. Res. Part F Traffic Psychol. Behav.* **2000**, *3*, 55–64. [CrossRef]

6. Mou, R.F.; Wang, C.Q. Study on pedestrian-vehicle conflict severity grade based on cloud theory. *J. Chang. Univ. (Nat. Sci. Ed.)* **2019**, *39*, 99–107.

7. Li, C.; Jiang, X.; Wang, W. A Simplified Car-following Model Based on the Artificial Potential Field. *Procedia Eng.* **2016**, *137*, 13–20. [CrossRef]

8. Liu, W.; Li, Z. Comprehensive predictive control method for automated vehicles in dynamic traffic circumstances. *IET Intell. Transp. Syst.* **2018**, *12*, 1455–1463. [CrossRef]

9. Li, L.H.; Jing, G.; Ji, X.K. Dynamic Driving Risk Potential Field Model Under the Connected and Automated Vehicles Environment and Its Application in Car-Following Modeling. *IEEE Trans. Intell. Transp. Syst.* **2020**, *23*, 122–141. [CrossRef]

10. Wang, J.; Wu, J.; Li, Y. The driving safety field based on driver–vehicle–road interactions. *IEEE Trans. Intell. Transp. Syst.* **2015**, *16*, 2203–2214. [CrossRef]

11. Qin, Y.Y.; Tang, H.H.; Li, S.Q. Capacity analysis of mixed traffic flow considering the influence of connected auxiliary driving equipment. *J. Shandong Univ. Sci. Technol. (Nat. Sci.)* **2023**, *42*, 120–128.

12. Jia, Y.F.; Qu, D.Y.; Zhao, Z.X. Car-following Decision-making and Model for Connected and Autonomous Vehicles Based on Safety Potential Field. *J. Transp. Syst. Eng. Inf. Technol.* **2022**, *22*, 85–97.

13. Qu, D.Y.; Meng, Y.M.; Wang, T. Car-following Model of Networked Autonomous Vehicle Based on Safety Characteristics of Molecular Force Field. *J. Transp. Syst. Eng. Inf. Technol.* **2023**, *23*, 33–41.

14. Ma, Y.L.; Qin, Q.; Dong, F.Q. Takeover Risk Assessment Model Based on Risk Field Theory Under Different Cognitive Secondary Tasks. *Automot. Eng.* **2024**, *46*, 9–17+28.

15. Huang, H.; Wang, J.; Fei, C. A probabilistic risk assessment framework considering lane-changing behavior interaction. *Sci. China (Inf. Sci.)* **2020**, *63*, 190203. [CrossRef]

16. Zheng, L.; Liu, W.; Zhai, C. A Dynamic Lane-Changing Trajectory Planning Algorithm for Intelligent Connected Vehicles Based on Modified Driving Risk Field Model. *Actuators* **2024**, *13*, 380. [CrossRef]

17. Chen, Z.; Zhao, W.L.; Guo, F.X. Lane Change Trajectory Planning of Intelligent Vehicle Considering Safety and Comfort. *J. Transp. Syst. Eng. Inf. Technol.* **2024**, *24*, 55–56.

18. Morse, P.M. Diatomic molecules according to the wave mechanics. *II. Vib. Levels. Phys. Rev.* **1929**, *34*, 57–64.

19. Nilsson, R. *Safety Margins in the Driver*; Uppsala University: Uppsala, Switzerland, 2001.

20. Ettinger, S.; Cheng, S.; Caine, B. Large Scale Interactive Motion Forecasting for Autonomous Driving: The Waymo Open Motion Dataset. In Proceedings of the 2021 IEEE/CVF International Conference on Computer Vision, Virtual, 11–17 October 2021; IEEE Computer Society: Piscataway, NJ, USA, 2021.

21. Wang, K.; Qu, D.; Shao, D.; Wei, L.; Zhang, Z. Research on Risk Quantification Methods for Connected Autonomous Vehicles Based on CNN-LSTM. *Appl. Sci.* **2024**, *14*, 11204. [CrossRef]

22. Ma, B.; Zhou, J.; Zhang, C. Risk Prediction Model for Tailings Ponds Based on EEMD-DA-LSTM Model. *Appl. Sci.* **2024**, *14*, 9141. [CrossRef]

23. Udurume, M.; Shakhov, V.; Koo, I. Comparative Analysis of Deep Convolutional Neural Network—Bidirectional Long Short-Term Memory and Machine Learning Methods in Intrusion Detection Systems. *Appl. Sci.* **2024**, *14*, 6967. [CrossRef]

24. Diaaeldin, A.; Zaher, M. Enhancing Road Safety: Leveraging CNN-LSTM and Bi-LSTM Models for Advanced Driver Behavior Detection. In Proceedings of the 2024 Intelligent Methods, Systems, and Applications (IMSA), Giza, Egypt, 13–14 July 2024; pp. 416–422.

25. Bian, S.; Li, H.; Wang, C.; Song, C.; Tang, Y. MSBF-LSTM: Most-significant Bit-first LSTM Accelerators with Energy Efficiency Optimisations. In Proceedings of the 2023 IEEE 31st Annual International Symposium on Field-Programmable Custom Computing Machines (FCCM), Marina Del Rey, CA, USA, 8–11 May 2023; p. 218.

26. Islam, M.; Lee, T. Wavelet Based Emotion Detection from Multi-channel EEG Using a Hybrid CNN-LSTM Model. In Proceedings of the TENCON 2022–2022 IEEE Region 10 Conference (TENCON), Hong Kong, China, 1–4 November 2022; pp. 1–6.

27. Xiong, W.; Han, L.; Qu, X. Bus Load Forecasting Based on Maximum Information Coefficient and CNN-LSTM Model. In Proceedings of the 2023 IEEE International Conference on Image Processing and Computer Applications (ICIPCA), Changchun, China, 11–13 August 2023; pp. 659–663.

28. Zhang, O.; Abdel-Aty, M.; Yue, L. CitySim: A Drone-Based Vehicle Trajectory Dataset for Safety-Oriented Research and Digital Twins. *Transp. Res. Rec.* **2024**, *2678*, 606–621. [CrossRef]

29. Chen, S.; Zhang, Q.; Lin, D.; Wang, S. A Class of Nonlinear Kalman Filters Under a Generalized Measurement Model with False Data Injection Attacks. *IEEE Signal Process. Lett.* **2022**, *29*, 1187–1191. [CrossRef]

30. Singh, A.K.; Kumar, S.; Kumar, N.; Radhakrishnan, R. Bayesian Approximation Filtering with False Data Attack on Network. *IEEE Trans. Aerosp. Electron. Syst.* **2022**, *58*, 876–988. [CrossRef]

31. Yuan, Y.; Qin, G.; Li, D.; Zhong, M.; Shen, Y.; Ouyang, Y. Real-Time Joint Filtering of Gravity and Gravity Gradient Data Based on Improved Kalman Filter. *IEEE Trans. Geosci. Remote Sens.* **2024**, *62*, 5925512. [CrossRef]

32. Kumar, G.; Naik, A.; Singh, K. Gaussian Filtering with Cyber-Attacked Data. *IEEE Signal Process. Lett.* **2024**, *31*, 546–550. [CrossRef]